ADVANCED ENERGY MATERIALS
www.advenergymat.de

Cobalt Polypyridyl Complexes as Transparent Solution-Processable Solid-State Charge Transport Materials

Muhammad K. Kashif, Rebecca A. Milhuisen, Michael Nippe, Jack Hellerstedt, David Z. Zee, Noel W. Duffy, Barry Halstead, Filippo De Angelis, Simona Fantacci, Michael S. Fuhrer, Christopher J. Chang, Yi-Bing Cheng, Jeffrey R. Long, Leone Spiccia, and Udo Bach**

Charge transport materials (CTMs) are traditionally inorganic semiconductors or metals. However, over the past few decades, new classes of solution-processable CTMs have evolved alongside new concepts for fabricating electronic devices at low cost and with exceptional properties. The vast majority of these novel materials are organic compounds and the use of transition metal complexes in electronic applications remains largely unexplored. Here, a solution-processable solid-state charge transport material composed of a blend of [Co(bpyPY4)](OTf)$_2$ and Co(bpyPY4)](OTf)$_3$ where bpyPY4 is the hexadentate ligand 6,6′-bis(1,1-di(pyridin-2-yl)ethyl)-2,2′-bipyridine and OTf$^-$ is the trifluoromethanesulfonate anion is reported. Surprisingly, these films exhibit a negative temperature coefficient of conductivity ($d\sigma/dT$) and non-Arrhenius behavior, with respectable solid-state conductivities of 3.0 S m^{-1} at room temperature and 7.4 S m^{-1} at 4.5 K. When employed as a CTM in a solid-state dye-sensitized solar cell, these largely amorphous, transparent films afford impressive solar energy conversion efficiencies of up to 5.7%. Organic–inorganic hybrid materials with negative temperature coefficients of conductivity generally feature extended flat π-systems with strong π–π interactions or high crystallinity. The lack of these features promotes [Co(bpyPY4)](OTf)$_{2+x}$ films as a new class of CTMs with a unique charge transport mechanism that remains to be explored.

Dr. M. K. Kashif, R. A. Milhuisen, Prof. Y.-B. Cheng, Prof. U. Bach
Department of Materials Science and Engineering
Monash University
Victoria 3800, Australia
E-mail: udo.bach@monash.edu

Prof. M. Nippe, D. Z. Zee, Prof. C. J. Chang, Prof. J. R. Long
Department of Chemistry
University of California, Berkeley
Berkeley, CA 94720, USA

Prof. M. Nippe, Prof. C. J. Chang
Chemical Sciences Division
Lawrence Berkeley National Laboratory
Berkeley, CA 94720, USA

Prof. M. Nippe, D. Z. Zee, Prof. J. R. Long
Materials Sciences Division
Lawrence Berkeley National Laboratory
Berkeley, CA 94720, USA

Prof. M. Nippe
Department of Chemistry
Texas A&M University
College Station, TX 77840, USA

Dr. J. Hellerstedt, Prof. M. S. Fuhrer
School of Physics and Monash Centre for Atomically Thin Materials
Monash University
Victoria 3800, Australia

Dr. J. Hellerstedt, Prof. M. S. Fuhrer
Center for Nanophysics and Advanced Materials
University of Maryland
College Park, MD 20742-4111, USA

Dr. N. W. Duffy, Dr. B. Halstead, Prof. U. Bach
CSIRO
Clayton South, Victoria 3169, Australia

Prof. F. De Angelis, Dr. S. Fantacci
Computational Laboratory for Hybrid/Organic Photovoltaics (CLHYO)
CNR-ISTM
Via Elce di Sotto 8 I-06123, Perugia, Italy

Prof. F. De Angelis
CompuNet
Istituto Italiano di Tecnologia
Via Morego 30, 16163 Genova, Italy

Prof. C. J. Chang
Department of Molecular and Cell Biology
University of California, Berkeley
Berkeley, CA 94720, USA

Prof. C. J. Chang
Howard Hughes Medical Institute
University of California, Berkeley
Berkeley, CA 94720, USA

Prof. J. R. Long
Department of Chemical and Biomolecular Engineering
University of California, Berkeley
Berkeley, CA 94720, USA

Prof. L. Spiccia
School of Chemistry
Monash University
Victoria 3800, Australia
E-mail: leone.spiccia@monash.edu

DOI: 10.1002/aenm.201600874

 © 2016 WILEY-VCH Verlag GmbH & Co. KGaA, Weinheim

1. Introduction

Organic solution-processable charge transport materials (CTMs) with metallic or semiconducting properties are nowadays commonly applied in electronic devices such as solar cells,[1,2] light-emitting diodes,[3] and plastic electronics.[4,5] Their intrinsic material properties, including charge mobility and conductivity, are often inferior to those of inorganic materials, such as copper or crystalline silicon. However, their low cost and processability enable them to be competitive alternatives when application requirements are less stringent and cost is the determining factor. They are compatible with a wide variety of deposition techniques, ranging from simple spin-coating to more sophisticated direct patterning methods, such as ink-jet printing. Fully printed electronic circuits can thus be created.[6] Organic solution-processable CTMs also play a vital role in high-performance perovskite solar cells, affording power conversion efficiencies beyond 20%.[7]

Few examples are known where transition metal complexes have found application as CTMs in electronic devices.[8,9] Traditionally these materials have been chosen for their superior light absorption and emission properties. Seminal examples include the thin copper phthalocyanine absorber layer used in Tang's archetypal two-layer organic solar cell[10] and highly luminescent iridium[9] and cobalt[11] complexes used in organic light-emitting diodes (OLEDs). Typically these thin layers are produced via vacuum deposition techniques rather than via solution processing methods.[12,13] Very recently, copper phenanthroline complexes have been successfully applied as a hole transport material in dye-sensitized solar cells (DSCs), thus pointing to the general prospect of developing transition metal complexes as an emerging class of CTMs.[14]

Here, we present a new class of solution-processable solid-state CTMs based on blends of the cobalt complexes $[Co(bpyPY4)](OTf)_2$ and $[Co(bpyPY4)](OTf)_3$, where bpyPY4 (**Figure 1**) corresponds to the hexadentate ligand 6,6′-bis(1,1-di(pyridin-2-yl)ethyl)-2,2′-bipyridine) and OTf^- is trifluoromethanesulfonate. These cobalt(II) and cobalt(III) complexes were synthesized as previously described.[15] We provide an analysis of the charge transport properties of materials made from these complexes and show that they can be used as solid-state conductors in DSCs, achieving energy conversion efficiencies of 5.7%.

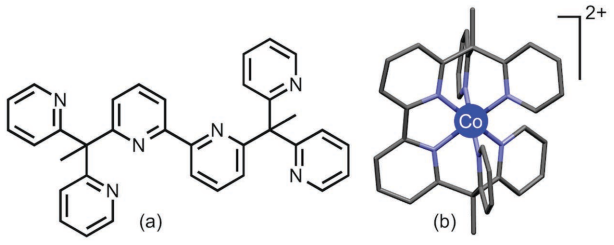

Figure 1. a) bpyPY4 ligand and b) spatial model of the $[Co(bpyPY4)]^{2+}$ cation derived from single-crystal X-ray crystallographic data obtained for $[Co(bpyPY4)](OTf)_2(CH_3CN)_2$.

2. Results and Discussion

The conductivity of a CTM is directly proportional to the product of mobility and number density of its charge carriers. In molecular CTMs, the latter can easily be controlled by deliberately tuning the ratio of oxidized versus reduced forms of the charge carrier. A typical example is the formation of doped films of the hole conductor spiro-OMeTAD (2,2′,7,7′-tetrakis(*N*,*N*-di-*p*-methoxyphenylamine)-9,9′-spirobifluorene) by spin-coating solutions containing spiro-OMeTAD and its oxidized form [spiro-OMeTAD](TFSI) ($TFSI^-$ = bis(trifluoromethanesulfonyl)-imide).[16]

Analogously, the conductivity of $[Co(bpyPY4)](OTf)_{2+x}$ films can be controlled by adding the one-electron oxidized complex $[Co(bpyPY4)](OTf)_3$ to film-forming solutions of $[Co(bpyPY4)](OTf)_2$. The variable x is defined as

$$x = \frac{\left[Co\left(bpyPY4\right)^{3+}\right]}{\left[Co\left(bpyPY4\right)^{2+}\right]+\left[Co\left(bpyPY4\right)^{3+}\right]} \quad (1)$$

Here, $[Co(bpyPY4)](OTf)_{2.33}$ (x = 0.33) corresponds to a film with a 2:1 molar ratio of $[Co(bpyPY4)](OTf)_2$ to $[Co(bpyPY4)](OTf)_3$.

Thin films of $[Co(bpyPY4)](OTf)_2$ and $[Co(bpyPY4)](OTf)_{2.33}$ were deposited onto interdigitated gold electrode arrays to characterize their conductive behavior (see the Experimental Section). Both types of films showed linear current–voltage characteristics (see Figure S1, Supporting Information), indicating good ohmic contact between the gold electrodes and the CTM. At room temperature, the pure $[Co(bpyPY4)](OTf)_2$ films showed a very low conductivity of 1.1×10^{-8} S m^{-1}. Addition of $[Co(bpyPY4)](OTf)_3$ dramatically increased the conductivity by up to eight orders of magnitude. The room-temperature conductivity of the $[Co(bpyPY4)](OTf)_{2.33}$ film was 3.0 S m^{-1}, whereas the room-temperature conductivity of a spiro-OMeTAD film with a typical molecular doping level of 10% was 4.8×10^{-5} S m^{-1}.

Temperature-dependent conductivity measurements were performed in order to further explore the dominant charge transport mechanism in $[Co(bpyPY4)](OTf)_{2+x}$ films (**Figure 2**). The resistivity versus temperature $\rho(T)$ plot surprisingly shows an almost linear decrease in resistivity for $[Co(bpyPY4)](OTf)_{2.33}$ upon cooling from 300 to 30 K, before it begins to level off at about 20 K (Figure 2a). The $[Co(bpyPY4)](OTf)_{2.33}$ films are more than twice as conductive at 4.5 K (7.4 S m^{-1}) than they are at room temperature (3.0 S m^{-1}). Similar temperature-dependent conductivity behavior was observed for $[Co(bpyPY4)](OTf)_2(BF_4)_{0.33}$ films fabricated from $[Co(bpyPY4)](OTf)_2$ solutions partially oxidized with $NOBF_4$ (see Figure S2, Supporting Information). This suggests that the combination of the $[Co(bpyPY4)]^{2+}$ and $[Co(bpyPY4)]^{3+}$ cations is responsible for both the improved conductivity and the temperature dependence of conductivity.

The temperature-dependent conductivity of CTMs in which thermally activated charge hopping between molecular species is the dominant charge transport mechanism can generally be described by the Arrhenius equation. For such CTMs,

© 2016 WILEY-VCH Verlag GmbH & Co. KGaA, Weinheim

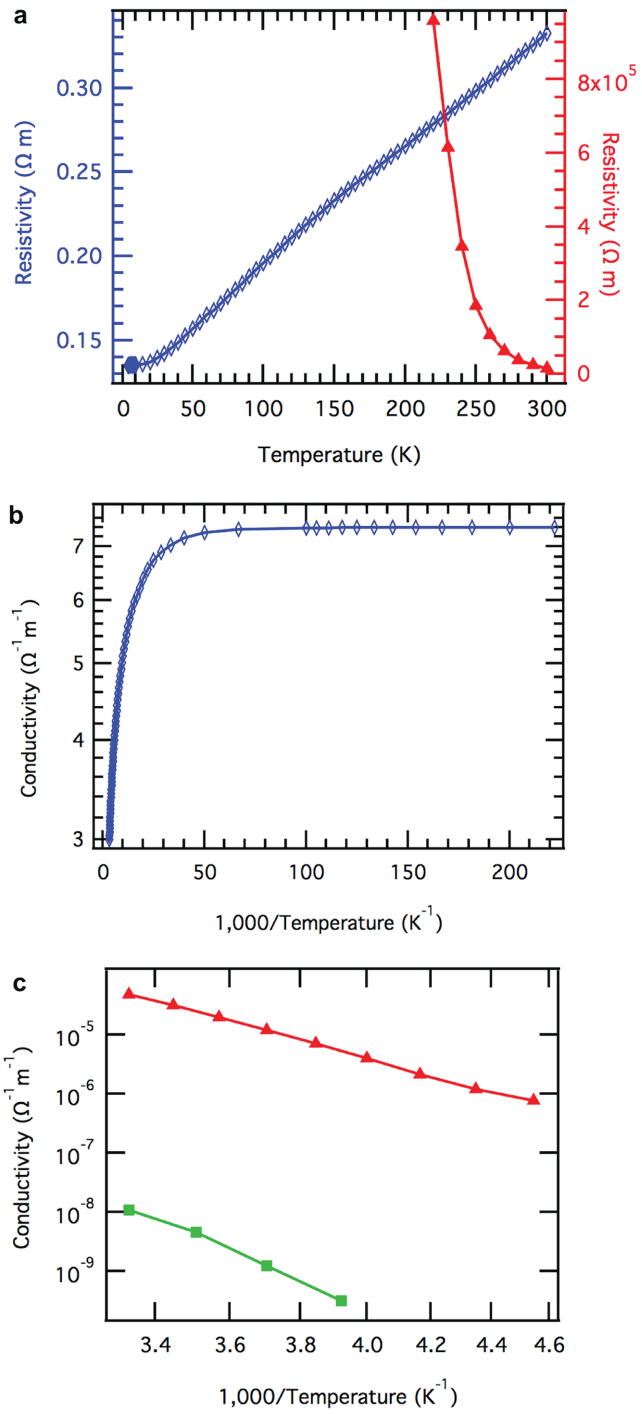

Figure 2. a) Resistivity of $[Co(bpyPY4)](OTf)_{2.33}$ (blue diamonds) and spiro-OMeTAD (red triangles) as a function of temperature, b) Arrhenius plot for the conductivity of $[Co(bpyPY4)](OTf)_{2.33}$, and c) Arrhenius plot for the conductivity of spiro-OMeTAD (red triangles) and $[Co(bpyPY4)](OTf)_2$ (green squares).

the classical Arrhenius plot of $\ln(\sigma)$ versus $1/T$ is linear with a negative slope that depends on the activation energy of the charge hopping process. The plot shown in Figure 2b clearly illustrates that non-Arrhenius-type transport is dominant for the

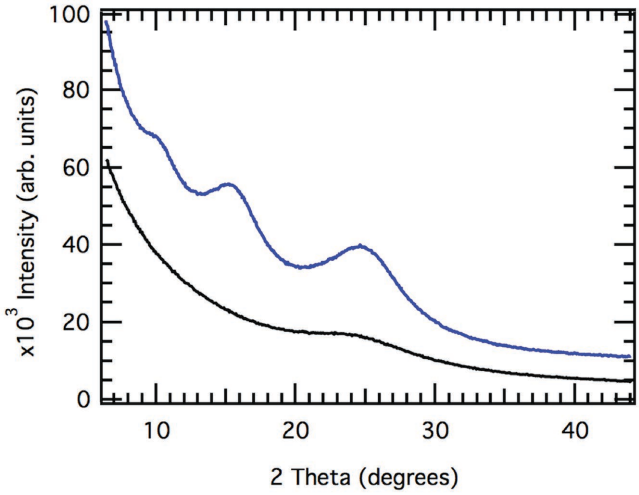

Figure 3. Grazing angle X-ray diffraction (GAXRD) of a 1.3 μm thick $[Co(bpyPY4)](OTf)_{2.33}$ film deposited onto a single crystalline Si substrate (blue). The diffractogram of the uncoated single crystalline Si substrate (black) is shown for comparison.

$[Co(bpyPY4)](OTf)_{2.33}$ films throughout the 4.5–300 K temperature range. This behavior is typically observed for metallic conductors and highly doped degenerate semiconductors showing band-like transport,[17,18] where the resistivity is dominated by acoustic phonon scattering. In contrast, the pure $[Co(bpyPY4)](OTf)_2$ films, which have only the cobalt(II) complex present, follow the classical temperature dependence expected for thermally activated charge transport systems, as is also found for doped films of the archetypal hopping-transport material spiro-OMeTAD (Figure 2c). A similar behavior has been reported for thin films of poly(3,4-ethylenedioxythiophene) (PEDOT), in which undoped films display thermally activated charge transport, while partially oxidized films whose charge is balanced by tosylate anions (PEDOT:Tos) exhibit negative temperature coefficients.[18] Interestingly, partially oxidized PEDOT films containing the polyelectrolyte polystyrene sulfonate (PEDOT:PSS) displayed thermally activated hopping transport even in the doped state. The differing temperature-dependent conductivities of the two partially oxidized PEDOT materials were attributed to the higher degree of crystallinity in PEDOT:Tos compared to the amorphous PEDOT:PSS films. The CTM studied here is fundamentally different from PEDOT:Tos, because the underlying charge transport phenomena in conducting polymers, such as polaron and bipolaron displacement, cannot occur in $[Co(bpyPY4)](OTf)_{2.33}$ films. The optical appearance of $[Co(bpyPY4)](OTf)_{2.33}$ films also indicates that this CTM is a glass-forming, rather than a crystalline, material (inset, Figure 4b).

Grazing-angle incident X-ray diffraction (GAXRD) analysis was used to further investigate the nanoscale morphology of $[Co(bpyPY4)](OTf)_{2.33}$ films on silicon wafers (**Figure 3**). Three very broad diffraction peaks can be identified at 10.5°, 15.5° and 25.0°. These peaks are absent on the GAXRD diffractogram of the silicon substrate. The observed GAXRD peak width suggests that the $[Co(bpyPY4)](OTf)_{2.33}$ film is mostly amorphous, with some indication of short-range order in the nanometer

© 2016 WILEY-VCH Verlag GmbH & Co. KGaA, Weinheim

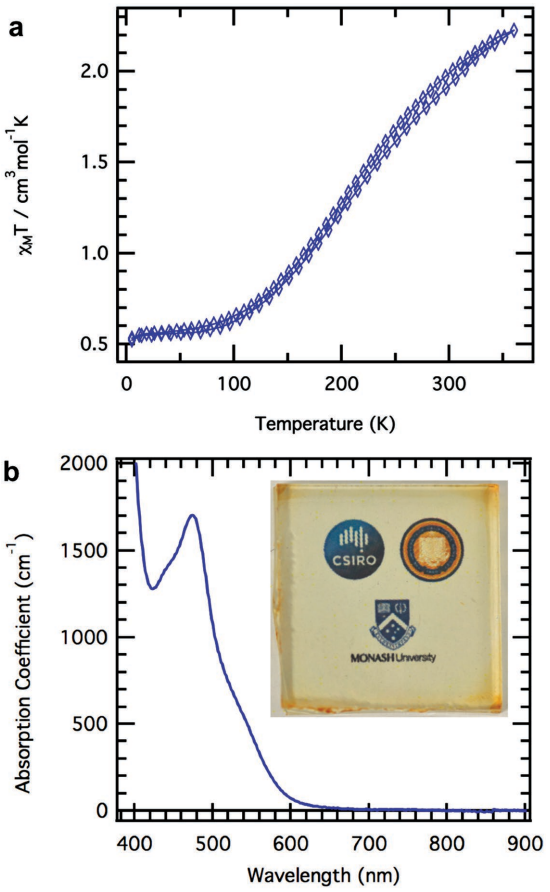

Figure 4. a) Variable-temperature magnetic susceptibility of [Co(bpyPY4)](OTf)$_{2.33}$, calculated on the basis of the [Co(bpyPY4)](OTf)$_2$ content and b) absorption coefficient of a [Co(bpyPY4)](OTf)$_{2.33}$ solid film. Inset: Image of institutional logos taken through a 0.83 µm thick [Co(bpyPY4)](OTf)$_{2.33}$ film applied on a TiO_2 coated conducting glass substrate.

range. Attempts to simulate the [Co(bpyPY4)](OTf)$_{2.33}$ thin film GAXRD diffractogram based on the available [Co(bpyPY4)](OTf)$_2$ single-crystal diffraction data coupled with peak broadening according to the Scherrer equation did not yield solutions with adequate fits.

Cobalt(II) polypyridyl complexes have been reported to undergo a high-spin to low-spin transition upon cooling.[19] In the presence of a trigonal prismatic ligand field, the Co^{2+} ion with a d^7 electron configuration can either adopt the low-spin state ($S = 1/2$) or high-spin state ($S = 3/2$). Magnetic measurements were performed to elucidate whether spin-crossover contributes to the unusual temperature-dependent conductivity behavior in [Co(bpyPY4)](OTf)$_{2.33}$ films. Room-temperature magnetic susceptibility measurements of the Co^{3+} complex, [Co(bpyPY4)](OTf)$_3$, confirmed its expected diamagnetic low-spin state. Temperature-dependent magnetic susceptibility ($\chi_M T$) data for [Co(bpyPY4)](OTf)$_{2.33}$ films indeed revealed that $\chi_M T$ continuously decreases from 350 to 100 K and levels off below 100 K (**Figure 4**a). This decrease in magnetic moment is consistent with a high-spin to low-spin transition of the Co^{2+} ions in [Co(bpyPY4)](OTf)$_{2.33}$. Importantly, the leveling of $\chi_M T$ at $T \leq 100$ K and the solid-state structure of [Co(bpyPY4)](OTf)$_2$ both indicate that spin-crossover transition is complete at 100 K, which precludes spin-crossover as an explanation of the low-temperature conductivity behavior from 100 to 10 K. The decrease in magnetic susceptibility observed for [Co(bpyPY4)](OTf)$_{2.33}$ upon cooling from 360 to 4 K closely matches the magnetic susceptibility changes that were observed for pure [Co(bpyPY4)](OTf)$_2$ (see Figure S3, Supporting Information), yet the observed temperature dependence of conductivity is fundamentally different for these materials.

The successful application of CTMs in optoelectronic devices often requires that the material itself does not absorb significant fractions of either generated or incident photons. In this regard, [Co(bpyPY4)](OTf)$_{2+x}$ films show exceptional optical properties. The molar extinction coefficients, ε, for [Co(bpyPY4)](OTf)$_2$ and [Co(bpyPY4)](OTf)$_3$ solutions in acetonitrile are below 200 $\text{M}^{-1}\ \text{cm}^{-1}$ throughout the entire visible spectrum (400–800 nm; see Figure S4, Supporting Information). For a 1.0 µm thick film, this translates to a transmission fraction of 83% or higher throughout the visible range, independent of the doping level (Figure 4b). Furthermore, the absence of broadening or shifts in the solution UV–vis and diffuse reflectance spectra of [Co(bpyPY4)](OTf)$_{2.33}$ either in solution or the solid-state, relative to an idealized combination of the individual cobalt(II) and cobalt(III) complexes suggests a lack of electronic coupling between these ions (see Figure S5, Supporting Information).

Hybrid density functional theory (DFT) calculations (B3LYP/6-311G*/CPCM) were performed to investigate whether differences in the electronic structure of $[Co(bpyPY4)]^{2+/3+}$ and $[Co(bpy)_3]^{2+/3+}$ can account for their distinctively different charge transport properties (see Figures S6 and S7, Supporting Information). Geometry optimization was carried out considering a low spin $^2[Co(bpyPY4)]^{2+}$ doublet and high spin $^4[Co(bpyPY4)]^{2+}$ quartet spin state and a closed shell singlet state, $^1[Co(bpyPY4)]^{3+}$, respectively. We calculate the quartet spin state $^4[Co(bpyPY4)]^{2+}$ to be favored by 0.16 eV over the $^2[Co(bpyPY4)]^{2+}$ doublet state at room temperature. This is in agreement with the magnetic susceptibility measurements shown in Figure 4a. Likewise, a quartet spin state was observed for the archetypical cobalt complex $[Co(bpy)_3]^{2+/3+}$ at room temperature[20] but with a larger quartet/doublet splitting of 0.21 eV. The highest occupied molecular orbital (HOMO) of the singlet $^1[Co(bpyPY4)]^{3+}$ complex is ligand-based, mainly localized on the bipyridyl unit of the bpyPY4 ligand, with little admixture of metal character. The lowest unoccupied molecular orbital (LUMO) and LUMO+1 are combinations of metal e_g (d_{x2-y2} and d_{z2}) states with ligand states. The frontier orbitals of the $^{2/4}[Co(bpyPY4)]^{2+}$ complexes are directly related to the HOMOs and LUMOs of $^1[Co(bpyPY4)]^{3+}$, as shown in Figure S6 (Supporting Information). The one-electron reduction of $^1[Co(bpyPY4)]^{3+}$ leads to $^2[Co(bpyPY4)]^{2+}$ with its singly occupied orbital corresponding to what was the LUMO of $^1[Co(bpyPY4)]^{3+}$. In $^4[Co(bpyPY4)]^{2+}$, formally obtained by splitting two electrons from a doubly occupied orbital of the ^{2}Co(II) complex, two unpaired electrons are localized in molecular orbitals, corresponding to the LUMO and LUMO+1 of $^1[Co(bpyPY4)]^{3+}$, while the lower-energy unpaired electron is partially delocalized across the ligand shell and the metal. This partial ligand character of the unpaired electrons is reflected in a total spin density on the metal of ≈2.7 e. While similar

© 2016 WILEY-VCH Verlag GmbH & Co. KGaA, Weinheim

admixtures of metal and ligand characters and charge delocalization were found for the frontier orbitals of $[Co(bpy)_3]^{2+/3+}$, the stabilization of the doublet state in $[Co(bpyPY4)]^{2+}$ may facilitate electron transfer by partly avoiding a spin-crossing barrier between the low-spin Co(III) and high-spin Co(II) species.

Novel CTMs have also been critically important for the advancement of emerging photovoltaic technologies. In DSCs, organic CTMs such as spiro-OMeTAD are often used to replace the commonly used corrosive, liquid electrolytes to form solid-state devices.[16,21,22] Application of spiro-OMeTAD in lead halide-based perovskite solar cells has recently increased their efficiency from 6.5% for an electrolyte-based device[23] to 20.1% for the spiro-OMeTAD-based solid-state analogue,[7] thus resulting in the fast evolving research field of perovskite solar cells (PSCs).

Our previous work demonstrated $[Co(bpyPY4)](OTf)_2$/$[Co(bpyPY4)](OTf)_3$ to be a viable redox mediator for the fabrication of liquid-electrolyte DSCs with exceptional stability under full sun illumination.[15] Energy conversion efficiencies for analogous devices reach 9.6% when used in conjunction with the classical organic sensitizer Y123 (see Table S1 and Figure S8, Supporting Information). Here, solid $[Co(bpyPY4)](OTf)_{2.33}$ films were employed in DSCs to demonstrate the applicability of this novel solid-state CTM in electronic devices. The solar cell fabrication method is described in the Experimental Section. Scanning electron microscopic imaging of DSC cross-sections showed good pore-filling and interpenetration into the dye-sensitized TiO_2 film by the solid $[Co(bpyPY4)](OTf)_{2.33}$ matrix (see Figure S9, Supporting Information).

Solid-state matrices of $[Co(bpyPY4)](OTf)_{2.33}$ were prepared neat and with both Li(TFSI) and 4-(trifluoromethyl)pyridine (TFMP) as additives. These additives were chosen because they have been shown to significantly improve efficiencies in solid-electrolyte DSCs using spiro-OMeTAD.[24] Here, we observed similar trends for solid-state DSCs employing $[Co(bpyPY4)](OTf)_{2.33}$ without and with additives, yielding efficiencies of 3.2% and 5.7%, respectively (**Table 1**). Respectable short-circuit current densities of 12.1 mA cm^{-2} and open-circuit voltages of 768 mV were obtained. Incident photon to electron conversion efficiencies (IPCEs) of up to 70% were recorded for solid-state $[Co(bpyPY4)](OTf)_{2.33}$ DSCs (see Figure S10, Supporting Information). Dissolution and subsequent NMR spectroscopic analysis of the $[Co(bpyPY4)](OTf)_{2.33}$ (with additives) solid-state matrix showed the residual acetonitrile to be ≈8 mass% (see Figure S11, Supporting Information). This is similar to the amount of solvent found in single crystals of $[Co(bpyPY4)](OTf)_3$ (11 mass%).

Table 1. Photovoltaic performance data for DSCs employing cobalt complexes as solid-state CTM and Y123 dye, under simulated sunlight (AM 1.5 G, 1000 W m^{-2}).

Complex	$[Co(bpyPY4)](OTf)_{2.33}$		$[Co(bpy)_3](OTf)_{2.33}$	
Additives	No[a)]	Yes[b)]	No[a)]	Yes[b)]
V_{OC} [mV]	654 ± 2	768 ± 1	694 ± 1	877 ± 5
J_{SC} [mA cm^{-2}]	7.07 ± 0.34	12.12 ± 0.26	0.02 ± 0.01	0.66 ± 0.20
FF	0.70 ± 0.01	0.62 ± 0.03	0.77 ± 0.02	0.73 ± 0.02
Efficiency, η [%]	3.23 ± 0.09	5.68 ± 0.06	0.02 ± 0.01	0.21 ± 0.05

Double-layer TiO_2 films (6.0 µm mesoporous TiO_2 (30 nm average particle size) and 4.0 µm scattering TiO_2 (400 nm average particle size)) were used for the fabrication of all DSCs. Platinum-coated conducting glass was used as counter electrode. The average performance with a standard deviation over four devices is provided; [a)]The solid-state charge transport matrix was formed from the following acetonitrile precursor solutions: 0.20 M Co(II) complex and 0.10 M Co(III) complex; [b)]The solid-state charge transport matrix was formed from the following acetonitrile precursor solutions: 0.20 M Co(II) complex, 0.10 M Co(III) complex, 0.05 M LiTFSI, and 0.50 M trifluoromethylpyridine.

In comparison, solid-state DSCs employing a blend of the $[Co(bpy)_3](OTf)_2$/$[Co(bpy)_3](OTf)_3$ (bpy = 2,2′-bipyridine) redox mediators yielded efficiencies of 0.02% in the absence and 0.22% in the presence of Li(TFSI) and TFMP (Table 1, **Figure 5**a). This poor performance is consistent with the low conductivity (<10^{-12} S m^{-1}) that was observed for solid $[Co(bpy)_3](OTf)_{2.33}$ films and also demonstrates that the exceptional performance of $[Co(bpyPY4)](OTf)_{2.33}$ films is not common to all cobalt polypyridyl complexes. Indeed, the 5.68% efficiency initially reported here for a solid-state cobalt complex hole transport material compares very favorably with the highest performance ever reported for a spiro-OMeTAD-based DSC of 7.7%, which is the result of continuous optimization of the initial reported efficiency of just 0.74% reported in 1998.

Intensity-modulated photovoltage spectroscopy, complemented by charge extraction experiments (see Figure S12a, Supporting Information) was used to determine the lifetime (Figure 5b) of photoinjected electrons in DSCs employing Co-bpyPY4 as liquid and solid-state electrolytes. Figure 5b reveals that the electron lifetime in the solid-state DSC is about 2.3 times shorter than for the liquid electrolyte Co-bpyPY4 DSCs, when the comparison is done at identical electron densities in the TiO_2 film. This can be explained in terms of the overall difference in the molar concentration of $[Co(bpyPY4)](OTf)_2$ in the liquid electrolyte (0.100 M) and solid-state CTM (0.55 M). The latter was estimated based on the densities of $[Co(bpyPY4)](OTf)_2$ and $[Co(bpyPY4)](OTf)_3$ derived from single-crystal X-ray diffraction data. Additional intensity-modulated photocurrent spectroscopy experiments revealed no major difference in electron transit times between liquid electrolyte and solid-state $[Co(bpyPY4)](OTf)_{2.33}$ DSCs (see Figure S12b, Supporting Information).

In conclusion, we have provided the first report of a transparent charge transport material based upon molecular cobalt complexes. Addition of $[Co(bpyPY4)](OTf)_3$ to $[Co(bpyPY4)](OTf)_2$ to form solid films of $[Co(bpyPY4)](OTf)_{2.33}$ resulted in a 10^8-fold increase in room temperature conductivity compared to pure $[Co(bpyPY4)](OTf)_2$ films. Temperature-dependent conductivity measurements revealed a negative temperature coefficient of conductivity for $[Co(bpyPY4)](OTf)_{2.33}$ films with respectable solid-state conductivities of 3.0 S m^{-1} at room temperature and 7.4 S m^{-1} at 4.5 K. While negative temperature coefficients are typically only observed for highly crystalline materials with extended planar π-systems or evidence of strong intermolecular coupling,[25] a morphology analysis of the $[Co(bpyPY4)](OTf)_{2.33}$ films by GAXRD revealed some low short-range ordering and no evidence of long-range crystallinity. This indicates that $[Co(bpyPY4)](OTf)_{2.33}$ is a unique transparent, non-crystalline CTM in which thermally activated charge hopping does not appear to be the prevailing charge

© 2016 WILEY-VCH Verlag GmbH & Co. KGaA, Weinheim

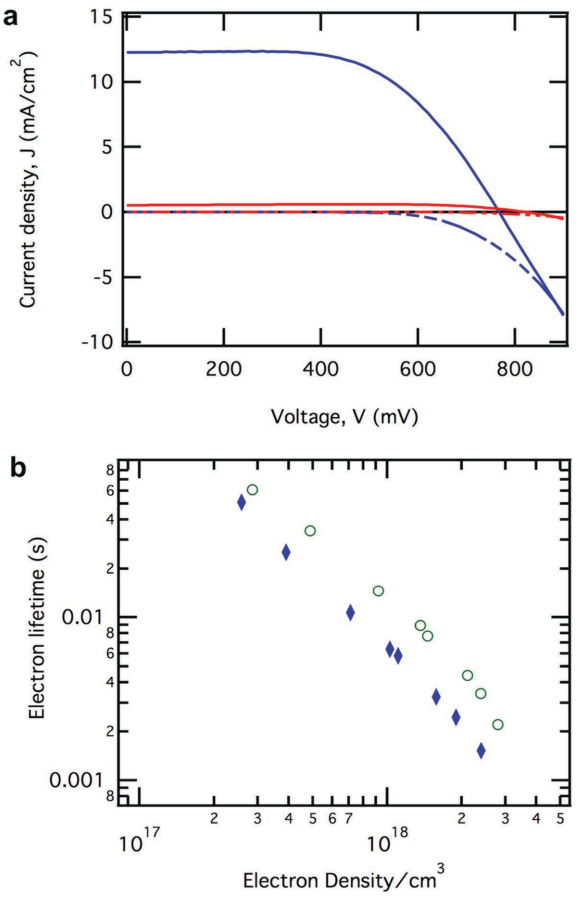

Figure 5. a) Current–density voltage curves measured under simulated AM1.5G (1000 W m^{-2}) sunlight (solid) and in the dark (dashed) for Y123-sensitized solid-state DSCs employing $[Co(bpyPY4)](OTf)_{2.33}$ (blue) and $[Co(bpy)_3](OTf)_{2.33}$ (red) as CTM. The solid-state charge transport matrices were formed from the following acetonitrile-based precursor solutions: $[Co(bpyPY4)](OTf)_{2.33}$; 0.20 M $[Co(bpyPY4)](OTf)_2$, 0.10 M $[Co(bpyPY4)](OTf)_3$, 0.05 M LiTFSI, and 0.50 M trifluoromethylpyridine. $[Co(bpy)_3](OTf)_{2.33}$; 0.20 M $[Co(bpy)_3](OTf)_2$, 0.10 M $[Co(bpy)_3](OTf)_3$, 0.05 M LiTFSI, and 0.50 M trifluoromethylpyridine. b) Electron lifetime as a function of electron density in the TiO_2 electrode for the solid-state $[Co(bpyPY4)](OTf)_{2.33}$ DSC (blue diamonds) shown in (a) and a liquid-electrolyte DSC with an identical electrolyte composition to the acetonitrile-based precursor solution described above (green circles).

transport mechanism. Further studies will be required to elucidate the unusual charge transport properties revealed in this work. Solid-state DSCs were fabricated to showcase the applicability of this novel class of solution-processable charge transport materials in optoelectronic devices. Respectable solar energy conversion efficiencies of 5.7% were achieved in this very first application of cobalt complex CTMs in DSCs.

3. Conclusion

To date, the use of transition metal complexes as electronic materials has been largely limited to specialized applications such as light-emitting diodes where such materials were selected based on their superior light emissive properties. Here, we have exposed the exceptional potential of transition metal complexes as solution-processable electronic charge transport materials, an area that has remained largely unexplored to date. Similar to their organic counterparts, CTMs based on transition metal complexes have almost unlimited variability of their chemical structure, providing ample opportunity for their solubility, morphology, conductivity, and energy levels to be fine-tuned, thus extending their applicability far beyond the DSC application demonstrated here.

4. Experimental Section

Preparation of Solutions for Conductivity Measurements: All solutions were prepared under inert conditions. $[Co(bpyPY4)](OTf)_2$ and $[Co(bpyPY4)](OTf)_3$ were synthesized according to literature procedures.[10] The $[Co(bpyPY4)](OTf)_{2.33}$ solution was prepared by dissolving $[Co(bpyPY4)](OTf)_2$ (175.4 mg, 0.20 M) and $[Co(bpyPY4)](OTf)_3$ (102.6 mg, 0.10 M) in acetonitrile (1 mL). Pure $[Co(bpyPY4)](OTf)_2$ solution was made by dissolving $[Co(bpyPY4)](OTf)_2$ (87.7 mg, 0.10 M) in acetonitrile (1 mL). The $[Co(bpy)_3](OTf)_{2.33}$ solution was prepared by dissolving $[Co(bpy)_3](OTf)_2$ (165.1 mg, 0.20 M) and $[Co(bpy)_3](OTf)_3$ (97.4 mg, 0.10 M) in acetonitrile (1 mL). The 10%-doped spiro-OMeTAD solution (0.10 M) was made following procedure as previously described by our group.[16]

Preparation of Samples for Conductivity Measurements: Interdigitated array (IDA) electrodes used to measure conductivity of the solid-state films were purchased from BAS-ALS. The electrodes comprised of 65 gold electrode pairs spaced 10 µm apart edge-to-edge on a quartz substrate. Each electrode was 5 µm wide, 2 mm long, and 90 nm thick. The electrodes also contained a non-conducting passivation layer which masked most of the substrate, exposing a very defined area of the interdigitated gold electrode pairs to the solid-state films. Prior to film deposition, the IDA electrodes were thoroughly rinsed with acetonitrile and dried under a stream of nitrogen. Under inert conditions, the $[Co(bpyPY4)](OTf)_{2.33}$, $[Co(bpyPY4)](OTf)_2$, $[Co(bpy)_3](OTf)_{2.33}$, and 10%-doped spiro-OMeTAD compound solutions were drop-cast onto the entire area including the passivation layer. As a result, smooth and homogeneous thin films formed on the 2 × 2 mm array of electrodes. An optical profilometer was used to accurately measure the thicknesses of the films on the IDA electrodes.

Room-Temperature Conductivity Measurements: The IDA devices were cut and mounted onto chip carriers. Electrical connections from the IDA electrodes to the gold attachment pads on the chip carriers were made via gold wire bonds. Devices were kept in a nitrogen-filled glovebox and the conductivity was measured on a potentiostat. The potentiostat was used to cycle the applied voltage between –0.8 and 0.8 V at a scan rate of 50 mV s^{-1} while monitoring the output current. The bulk conductivities, σ, of the thin films were calculated from the slope of the acquired current–voltage curves and by applying the relationship $\sigma = (I/V)(d/((2n-1)lh))$ [S m^{-1}] (where I is the current measured, V is the applied bias voltage, d is the electrode spacing, n is the number of electrode pairs, l is the electrode length, and h is the film thickness).

Variable Temperature Conductivity Measurements: Conductivity measurements over the temperature range 4.5–300 K were performed using a Quantum Design Physical Property Measurement System (PPMS). IDA samples were loaded into the sample chamber of the PPMS and secure electrical connections were made via the gold connector pins of the chip carrier. IDAs were sealed in the sample chamber at a pressure of 10^{-2} Torr. At each equilibrated temperature (starting from 300 K and cooling down to 4.5 K), IDAs were cycled between –0.01 and 0.01 V at a scan rate of 20 mV s^{-1} and the conductivity calculated as previously described.

Magnetic Measurements: Magnetic susceptibility measurements were performed using a Quantum Design MPMS2 SQUID magnetometer. Magnetic samples were prepared by adding powdered crystalline compounds to a 7 mm diameter quartz tube with a raised quartz platform. The sample was restrained with icosane and sealed in

© 2016 WILEY-VCH Verlag GmbH & Co. KGaA, Weinheim

the quartz tube. Direct current (dc) magnetic susceptibility data measurements were performed at temperatures ranging from 2 to 300 K using applied fields of 1000 Oe. All data were corrected for diamagnetic contributions from the icosane and core diamagnetism, estimated using Pascal's constants.[26]

Solar Cell Fabrication: For *I–V* characterization, working electrodes (4 × 4 mm in dimension) comprised a 6.0 µm thick transparent mesoporous layer consisting of 30 nm sized TiO_2 particles and a 4.0 µm thick scattering layer of 400 nm sized TiO_2 particles that were screen-printed onto fluorine doped SnO_2 (FTO) conducting glass. For IMVS/IMPS measurements, working electrodes comprised only a 4.0 µm thick transparent layer of 30 nm sized TiO_2. These working electrodes were sintered at 500 ± 25 °C for 15 min after which they were immersed into a 20×10^{-3} M $TiCl_4$ solution at 70 °C for 30 min. The $TiCl_4$-treated TiO_2 working electrodes were reheated with a heat gun at 500 ± 25 °C for 30 min and immersed into a 1×10^{-6} M solution of 3-{6-{4-[bis(2′,4′-dihexyloxybiphenyl-4-yl)amino-]phenyl}-4,4-dihexyl-cyclopenta-[2,1-*b*:3,4-*b*′]dithiphene-2-yl}-2-cyanoacrylic acid (Y123) in acetonitrile:toluene (1:1) for 24 h. Counter electrode FTO substrates were platinized via thermal decomposition of a 10×10^{-3} M chloroplatinic acid solution in isopropanol at 400 °C for 14 min. The working and counter electrodes were fused together with a 25 µm hot-melt surlyn gasket, forming a compartment into which the acetonitrile solutions containing the complexes (composition given earlier) was filled through an injecting hole via a back-filling technique and the aid of vacuum. For solid-state cells, the acetonitrile solution was repeatedly back-filled and the solvent removed under vacuum. This was followed by a 4 h drying period on a 70 °C hotplate, ensuring complete removal of acetonitrile solvent. A glass cover slip backed with hot-melt surlyn was then used to seal the injecting hole. Cells were tested immediately after device fabrication.

Supporting Information

Supporting Information is available from the Wiley Online Library or from the author.

Acknowledgements

This study was supported by the Australian Government through the Australian Research Council (ARC) and the Australian Renewable Energy Agency (ARENA). The CSIRO provided support through the OCE Science Leader program. M.S.F. was supported by an ARC Laureate Fellowship FL120100038. J.H. was supported by U.S. NSF Award No. DMR-11-05224. Contributions of M.N. and C.J.C. were supported by DOE/LBNL DE-AC02-05CH11231 and FWP CH030201. C.J.C. is an Investigator with the Howard Hughes Medical Institute. Contributions of D.Z.Z. and J.R.L. were supported by NSF Grant No. CHE-1464841. The authors thank Prof. Keith Murray and Dr. Boujemaa Moubaraki for the magnetic and conductivity measurements and valuable discussions. Part of this work was performed at the Melbourne Centre for Nanofabrication (MCN) in the Victorian Node of the Australian National Fabrication Facility (ANFF).

Received: April 27, 2016
Revised: June 22, 2016
Published online:

[1] S. Günes, H. Neugebauer, N. S. Sariciftci, *Chem. Rev.* **2007**, *107*, 1324.
[2] B. C. Thompson, M. J. Fréchet, *Angew. Chem., Int. Ed.* **2008**, *47*, 58.
[3] A. P. Kulkarni, C. J. Tonzola, A. Babel, S. A. Jenekhe, *Chem. Mater.* **2004**, *16*, 4556.
[4] A. C. Arias, J. D. MacKenzie, I. McCulloch, J. Rivnay, A. Salleo, *Chem. Rev.* **2010**, *110*, 3.
[5] S. R. Forrest, *Nature* **2004**, *428*, 911.
[6] R. R. Søndergaard, M. Hösel, F. C. Krebs, *J. Polym. Sci., Part B: Polym. Phys.* **2013**, *51*, 16.
[7] W. S. Yang, J. H. Noh, N. J. Jeon, Y. C. Kim, S. Ryu, J. Seo, S. I. Seok, *Science* **2015**, *348*, 1234.
[8] S. A. Getty, C. Engtrakul, L. Wang, R. Liu, S. Ke, H. U. Baranger, W. Yang, M. S. Fuhrer, L. R. Sita, *Phys. Rev. B* **2005**, *71*, 241401.
[9] H. Xu, R. Chen, Q. Sun, W. Lai, Q. Su, W. Huang, X. Liu, *Chem. Soc. Rev.* **2014**, *43*, 3259.
[10] C. W. Tang, *Appl. Phys. Lett.* **1986**, *48*, 183.
[11] X. Ren, B. D. Alleyne, P. I. Djurovich, C. Adachi, I. Tsyba, R. Bau, M. E. Thompson, *Inorg. Chem.* **2004**, *43*, 1697.
[12] E. V. A. Premalal, G. R. R. A. Kumara, R. M. G. Rajapakse, M. Shimomura, K. Kurakami, A. Konno, *Chem. Commun.* **2010**, *46*, 3360.
[13] I. A. Rutkowska, A. Andrearczyk, S. Zoladek, M. Goral, K. Darowicki, P. J. Kulesza, *J. Solid State Electrochem.* **2011**, *15*, 2545.
[14] M. Freitag, Q. Daniel, M. Pazoki, K. Sveinbjörnsson, J. Zhang, L. Sun, A. Hagfeldt, G. Boschloo, *Energy Environ. Sci.* **2015**, *8*, 2634.
[15] M. K. Kashif, M. Nippe, N. W. Duffy, C. M. Forsyth, C. J. Chang, J. R. Long, L. Spiccia, U. Bach, *Angew. Chem., Int. Ed.* **2013**, *52*, 5527.
[16] U. B. Cappel, T. Daeneke, U. Bach, *Nano Lett.* **2012**, *12*, 4925.
[17] E. Bustarret, C. Marcenat, P. Achatz, J. Kačmarčik, F. Lévy, A. Huxley, L. Ortéga, E. Bourgeois, X. Blase, D. Débarre, J. Boulmer, *Nature* **2006**, *444*, 465.
[18] O. Bubnova, Z. U. Khan, H. Wang, S. Braun, D. R. Evans, M. Fabretto, P. Hojati-Talemi, D. Dagnelund, J. Arlin, Y. H. Geerts, S. Desbief, D. W. Breiby, J. W. Andreasen, R. Lazzaroni, W. M. Chen, I. Zozoulenko, M. Fahlman, P. J. Murphy, M. Berggren, X. Crispin, *Nat. Mater.* **2014**, *13*, 190.
[19] R. Hogg, R. G. Wilkins, *J. Chem. Soc.* **1962**, 341.
[20] I. Krivokapic, M. Zerara, M. L. Daku, A. Vargas, C. Enachescu, C. Ambrus, P. Tregenna-Piggott, N. Amstutz, E. Krausz, A. Hauser, *Coord. Chem. Rev.* **2007**, *251*, 364.
[21] U. Bach, D. Lupo, P. Comte, J. E. Moser, F. Weissörtel, J. Salbeck, H. Spreitzer, M. Grätzel, *Nature* **1998**, *395*, 583.
[22] T. Inabe, H. Tajima, *Chem. Rev.* **2004**, *104*, 5503.
[23] J. H. Im, C. R. Lee, J. W. Lee, S. W. Park, N. G. Park, *Nanoscale* **2011**, *3*, 4088.
[24] G. Boschloo, L. Häggman, A. Hagfeldt, *J. Phys. Chem. B* **2006**, *110*, 13144.
[25] E. Coronado, J. R. Galán-Mascarós, C. J. Gómez-García, V. Laukhin, *Nature* **2000**, *408*, 447.
[26] G. A. Bain, J. F. Berry, *J. Chem. Educ.* **2008**, *85*, 532.

© 2016 WILEY-VCH Verlag GmbH & Co. KGaA, Weinheim